



Application of the Taguchi method to areal roughness-based surface topography control by waterjet treatments

Jing Xie^{a,*}, Yang Qiao^a, Zu'an Wang^a, Yuanshen Qi^b, Qingfeng Xu^c, Keren Shemtov-Yona^{d,e}, Pengwan Chen^a, Daniel Rittel^d

^a State Key Laboratory of Explosion Science and Technology, Beijing Institute of Technology, Beijing, 100081, China

^b Department of Materials Science and Engineering, Guangdong Technion - Israel Institute of Technology, Shantou 515063, China

^c Hospital of Stomatology, Shantou University Medical College, Shantou 515063, China

^d Faculty of Mechanical Engineering, Technion - Israel Institute of Technology, 32000 Haifa, Israel

^e The Maurice and Gabriela Goldschleger School of Dental Medicine, Department of Oral Biology, Tel Aviv University, Tel Aviv, Israel

ARTICLE INFO

Keywords:

Waterjet

Ti6Al4V

Areal roughness

Microstructure

Hardness

Taguchi

ABSTRACT

Pure waterjet surface treatment without abrasive particles has a promising application in the biomedical field, because it induces compressive residual stresses on a metal surface and never leaves the tiny hard particles. In this work, the influence of operation pressure, standoff distance and the number of paths of the waterjet on the surface topography as well as the hardness was studied using the Taguchi method. The results showed that the most essential parameter is the operation pressure. By tuning the operation pressure from 100 to 300 MPa, the surface of Ti6Al4V specimens can be smoothed, roughened or damaged; when the surface layer is eroded, the new-born surface exhibits a clear stochastic nature accompanied by microvoids. The standoff distance benefits finer controlling the height parameters, whilst the number of paths affects the waviness. The hardening effect generated by the waterjet impingement extends to a few hundred-micron depth of the specimens, and the peak value of microhardness was found at a depth of 70 μm , which is an increase by greater than 20 %. The roughness parameters of Arithmetical mean height (S_a), Skewness (S_{sk}), Auto-correlation length (S_{al}), and Developed interfacial area ratio (S_{dr}) as a set are recommended to characterize the biomaterial's surface. The present research results promote the application of waterjet treatment in the field of fine-tuning biomaterial surface morphology.

1. Introduction

The surface topography of the implant significantly influences the bone response [1,2]. There are two stages (short/long) of biological response after implantation [3]. One is the short-term response that a fibrous soft tissue is formed and capsules around the implant, and another response directly relates to bone-implant contact without the connective tissue layer, known as osseointegration [4]. The surface topography plays an important role in the biomechanical fixation between the implant and the soft fibrous tissue at the early stage of implantation. Meanwhile, the rate and quality of osseointegration that determine the long-term success of the clinic implantation are also affected by the surface topography [5]. The demand for specific surface finishes of biomedical devices [6] drives researchers to develop efficient surface modification methods.

Waterjet technology that places a sample under the waterjet itself and subjects it to the water pressure in the air or underwater is one of the promising methods [7,8]. As one of the fastest-growing technologies, the waterjet can machine (cut, drill and mill, clean, remove) almost any material [9]. Waterjet is used in a variety of fields from automotive and aerospace to medical and the food industries [10]. Particularly, pure waterjet induces compressive residual stress to enhance fatigue strength [11], and never leaves tiny residues (hard particles) on a metal surface compared to the abrasive waterjet, it holds tremendous promise in the medical industry [7,11].

Taylor proposed the modification of metallic substrates through the use of high-pressure pure waterjet technology in early 1995 [12]. The essence of his proposal lies in the controlled erosion of the substrate, to achieve minimal thickness loss. Arola and McCain [13] are recognized pioneers in the utilization of abrasive waterjet peening, particularly in

* Corresponding author.

E-mail address: jxie@bit.edu.cn (J. Xie).

<https://doi.org/10.1016/j.apsadv.2023.100548>

Received 7 October 2023; Received in revised form 3 December 2023; Accepted 4 December 2023

2666-5239/© 2023 The Author(s). Published by Elsevier B.V. This is an open access article under the CC BY-NC-ND license (<http://creativecommons.org/licenses/by-nc-nd/4.0/>).

the context of surface preparation for metal orthopedic implants. Notably, Barriuso et al. [7] and Lieblisch et al. [11] conducted analyses to assess the feasibility and viability of employing pure waterjet processing to roughen the surface of the metallic biomaterial Ti6Al4V alloy. Xie and Rittel conducted a series of simulation work to predict the surface profile by using the pure waterjet with/without considering the initial surface roughness [14–18]. Table 1 summarizes the current research issues concerning the waterjet peened surface obtained from the literature, which is not limited to the biomaterial Ti6Al4V alloy.

Most researchers only consider the height parameters (R_a , R_z), and the parameters for characterizing the horizontal direction of a surface profile are seldom reported. In the recent 5 years, a few researchers have realized the limitations of using line roughness parameters and started to adopt the concept of areal roughness and investigate its influence on the biocompatibility of implants [34–40]. The areal parameters of a waterjet peened surface, however, have not been analyzed comprehensively.

Moreover, the influence of waterjet processing parameters on surface topography is also one of the hot topics. As per Table 1, a higher pressure, a closer standoff distance or multiple impacts would all benefit roughening the surface, but how to obtain a desired surface topography, specifically a desired roughness value, with waterjet has not been answered yet. The Taguchi method [41] (a statistical technique to optimize the performance of the products or process) is therefore used in the current work to design experiments and find out which parameters are suitable for generating the desired surface profile.

The Taguchi method utilizes orthogonal arrays to efficiently explore the parameter space with minimal experiments [42,43]. A loss function quantifies the deviation between experimental and desired values, transformed into a signal-to-noise (S/N) ratio. The S/N ratio, categorized as lower-the-better, higher-the-better, or nominal-the-better, identifies optimal process parameters with the highest S/N ratio. Statistical analysis of variance (ANOVA) determines the significance of process parameters, enabling the prediction of the optimal combination. With the S/N and ANOVA analyses, the optimal combination of the process parameters can be predicted.

Ti6Al4V is one of the most common titanium-based implant biomaterials because of its lightness and good mechano-chemical properties [44–46]. The attractive mechanical (i.e., lower Young's modulus than cobalt alloys and stainless steels) and physical (i.e., low weight) properties of Ti6Al4V alloy, as well as its advantageous tribological (i.e., high corrosion resistance) and biological (i.e., excellent soft and hard tissue biocompatibility) performance, make Ti6Al4V alloy very appealing for biomedical products such as orthopedic and dental implants [44–51]. Therefore, the effect of pure waterjet on Ti6Al4V is

investigated, looking for an optimal processing parameter for generating and controlling desired surface roughness. Special emphasis is devoted to the areal characterization of the surface profile, the microstructure of the treated surface and the subsurface hardening. Information on these aspects is lacking despite its relevance to the performance of Ti6Al4V as an implant material. A discussion of waterjet treated surface in the osseointegration is made in the last section.

2. Materials and methods

2.1. Materials and sample preparation

The material subjected to waterjet in this study was a commercial Ti6Al4V (Botai Metal Material Co., LTD, Baoji, China) with a chemical composition of 5.97 wt % Al, and 4.03 wt % V and Ti (balance). The XUCHANG AC 5-axis waterjet system with a CUX-400H ultra-high pressure intensifier pump was used to conduct the waterjet experiment (Fig. 1). The intensifier pump can develop a jet pressure of up to 400 MPa. A nozzle assembly with a sapphire orifice of 0.2 mm in diameter (D) was utilized. The jet traverse speed (v) was set as 800 mm min⁻¹.

The operating pressure (P_w), the standoff distance (SOD) and the number of jet passes (zoom in on Fig. 1(a)) are the primary processing parameters that affect the final surface topography [19,26,52]. Herein one pass is defined as the nozzle moving back and forth once, thus it is proportional to the exposure time. In order to investigate how these parameters influence the surface roughness, the Taguchi method was adopted [43]. Initial single pass trials (not presented here) were carried out with a wide range of parameters: operating pressure between 100 MPa and 300 MPa; standoff distance between 50 mm and 150 mm; the number of jet passes between 2 and 8.

Based on these initial trials, Taguchi's L9 orthogonal array was designed, and a total of 9 different parametric conditions were selected in the present study as listed in Table 2. Factor 1 (F1) stands for the P_w , which has three levels (100/200/300 MPa); factor 2 (F2) is the SOD , and its three levels are 50, 100 and 150 mm, respectively; and the number of parth is the third factor (F3), and 2, 5 and 8 are the three levels selected for this study.

Usually, for a 3-factor 3-level test, 27 (3^3) trials should be carried out with a standard orthogonal array. But with Taguchi's design, it can be reduced to 9 cases which can effectively save time and cost. In this work, each trial conducted three tests in order to avoid bias. A more detailed description of the Taguchi method can be found in Appendix A.

Table 1
Roughness parameters concerning the waterjet peened surface.

Reference	Target material	Pressure (MPa)	Standoff distance (mm)	Path number	R_a (μm)	Other parameters
Ref [7]	Ti6Al4V	360	2	1	11/12 \pm 2	R_z
Ref [11]	Ti6Al4V	240/360	2	1	1.3–23.3	W_a
Ref [19]	Ti6Al4V	140/210/280	150	2	1.0/2.2/2.4	R_z , R_{pk} , R_{vk}
Ref [20]	Ti6Al4V	138/207	13–152	4/8	0.1–1	
Ref [21]	Ti6Al4V	600	12.7/25.4/38.1/50.8/63.5	1	3.8/4/3.4/2/1	R_z
Ref [22]	Ti6Al4V	275/414/600	12.7–139.7	1	0–15	R_z
Ref [23]	Ti6Al4V	138/207/345	5/20/50	4	3.2–17.4	R_k , R_{pk} , R_{vk}
Ref [24]	Stainless steel 304	100/200/300	30	2/4/6	0.5–9.0	
Ref [25]	Stainless steel 304	100/200/300	30	3/6/9	8–11	R_z , R_{pk} , R_{vk}
Ref [26]	Stainless steel 304	200	30	2/4/6	0.78–4.86	
Ref [27]	Al6061-T6	276	12.7/25.4/38.1	1	4/3/3	R_q , R_z
Ref [28]	Al7475	0.04/0.05	10/25	1–4	5–7	
Ref [29]	Al5005	50/100/150	20/40/60	1/2/3	0.53–16.41	
Ref [30]	Al5052	15/20/25/30	10–60	1	1–22	R_z
Ref [31,32]	Al-MMC	34.5	25.4	1	5–35	R_v , R_p
Ref [33]	18CrNiMo7–6 steel	300	10	1	0.08–0.25	

- R_a is referred to as the arithmetic mean roughness, while W_a is referred to as the arithmetic mean waviness for the waviness profile.
- R_q is referred to as the root-mean-square roughness.
- R_z is the maximum height of a profile; R_p and R_v are the maximum peak height and valley depth, respectively.
- R_k is the core roughness depth; R_{pk} and R_{vk} are the reduced peak height and valley depth, respectively.

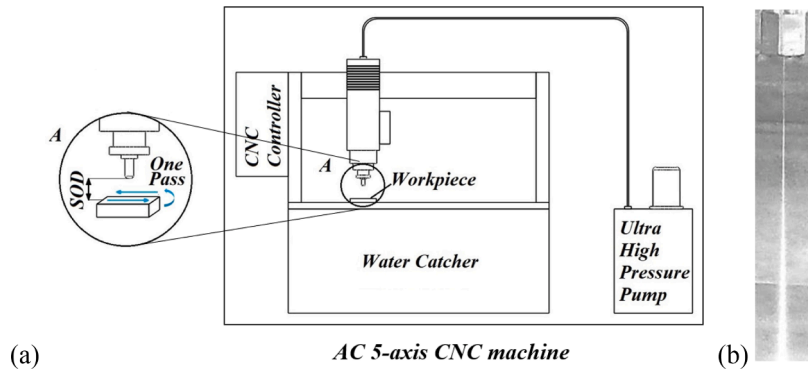


Fig. 1. (a) Schematic diagram of waterjet system and (b) Optical image of waterjet in the air (without final region).

Table 2
L9 orthogonal array and experiments design.

Case No.	Control factors and levels			Experiment conditions		
	F1	F2	F3	Pw (MPa)	SOD (mm)	n
1#	1	1	1	100	50	2
2#	1	2	2	100	100	5
3#	1	3	3	100	150	8
4#	2	1	2	200	50	5
5#	2	2	3	200	100	8
6#	2	3	1	200	150	2
7#	3	1	3	300	50	8
8#	3	2	1	300	100	2
9#	3	3	2	300	150	5

2.2. Areal roughness parameters

There are five categories of roughness parameters: height, spatial, hybrid, functional and feature parameters [53]. Seven height parameters were used to characterize the height of the surface profile:

arithmetical mean height (Sa), root mean square height (Sq), skewness (Ssk), kurtosis (Sku), maximum peak height (Sp), maximum pit height (Sv) and maximum height (Sz). The spacing between features was evaluated by the auto-correlation function (Sal).

The most relevant roughness parameter to the area of a real surface is the developed surface area ratio (Sdr). The sloped triangles contribute to Sdr being more accurate than the sloped quadrilaterals, indicating that Sdr is tightly connected to the RMS gradient and, thus, Sdq is measured as well.

Functional parameters are commonly applied for the evaluation of honed surfaces and thus provide a tool for the evaluation of properties that are associated with the material ratio curve [54]. Thus, Spk may represent the nominal height of the material that may be removed during a running-in operation. Sk represents the core roughness of the surface over which a load may be distributed after the surface has been run in. Svk is a measure of the valley depths below the core roughness and may be related to lubricant retention and debris entrapment.

Arithmetic mean peak curvature (Spc) is one of the feature parameters which has a proportional relationship to the shear stress between

Table 3
Area roughness parameters (ISO 25178-2).

No.	Category	Symbol	Parameters	Definition
1	Height	Sa (μm)	Arithmetical mean height	$Sa = \frac{1}{A} \iint_A z(x,y) dx dy$
2		Sq	Root mean square height	$Sq = \sqrt{\frac{1}{A} \iint_A z^2(x,y) dx dy}$
3		Ssk	Skewness	$Ssk = \frac{1}{Sq^3} \frac{1}{A} \iint_A z^3(x,y) dx dy$
4		Sku	Kurtosis	$Sku = \frac{1}{Sq^4} \frac{1}{A} \iint_A z^4(x,y) dx dy$
5		Sp (μm)	Maximum peak height	$Sp = \max_A z(x,y)$
6		Sv (μm)	Maximum valley height	$Sv = \min_A z(x,y) $
7		Sz (μm)	Maximum height	$Sz = Sp + Sv$
8	Spatial	Sal (μm)	Auto-correlation length	$ACF(\tau_x, \tau_y) = \frac{\iint_A z(x,y)z(x-\tau_x, y-\tau_y) dx dy}{\iint_A z(x,y)^2 dx dy}$ $Sal = \min \sqrt{\tau_x^2 + \tau_y^2}$
9	Hybrid	Sdr (%)	Developed interfacial area ratio	$Sdr = \frac{1}{A} \left[\iint_A \left(\sqrt{1 + \left(\frac{\partial z(x,y)}{\partial x} \right)^2 + \left(\frac{\partial z(x,y)}{\partial y} \right)^2} - 1 \right) dx dy \right]$
10		Sdq	Root mean square gradient	$Sdq = \sqrt{\frac{1}{A} \iint_A \left[\left(\frac{\partial z(x,y)}{\partial x} \right)^2 + \left(\frac{\partial z(x,y)}{\partial y} \right)^2 \right] dx dy}$
11	Functional	Sk (μm)	Core height	The difference of heights at the areal material ratio values 0 % and 100 % on the equivalent line
12		Spk (μm)	Reduced peak height	The mean height of peaks above the core surface
13	Feature	Svk (μm)	Reduced valley depth	The arithmetical mean of the reduced valley depth of the areal material ratio curve
14		Spc (μm^{-1})	Arithmetic mean peak curvature	$Spc = -\frac{1}{2} \frac{1}{n} \sum_{k=1}^n \left(\frac{\partial^2 z(x,y)}{\partial x^2} + \frac{\partial^2 z(x,y)}{\partial y^2} \right)$

two contact surfaces (e.g. implant and bone) [55], thus it can be used to characterize the effective surface area of a rough surface.

Surface morphologies and the related 14 parameters were therefore measured and calculated using a noncontact optical profilometer (Rtec UP-Lambda, Rtec Universal Profilometer, California, USA) within a $300 \times 300 \mu\text{m}$ definition area. Table 3 summarizes descriptions of all the parameters used. Three topographical measurements were performed for each analyzed surface.

2.3. Signal-to-noise ratio

The signal-to-noise (S/N) ratio was calculated to obtain the best set of the processing conditions arrangement for obtaining the desired surface roughness. The term “signal” and “noise” represents the desirable and undesirable value for the output characteristics, respectively. There are 3 types of S/N ratios depending on the desired performance response: the larger the better; the smaller the better; the nominal the best. Nominal the best was used in this study, because the surface parameters are desired to be suitable (nominal target) for good bone osseointegration, neither larger nor smaller. The signal-to-noise ratio is calculated as follows:

$$\left(\frac{S}{N}\right)_T = 10 \log \left(\frac{\bar{y}^2}{\sigma^2} \right) \quad (1)$$

where $\bar{y} = \frac{1}{k} \sum_{i=1}^k y_i$, and $\sigma = \sqrt{\sum_{i=1}^k \frac{(y_i - \bar{y})^2}{k-1}}$, k is the number of measurements in an orthogonal array trail and y_i is the measured roughness value in a trail.

Unfortunately, which surface roughness is ideal for osseointegration is still unknown despite the advancement of biomaterials [56]. Thus, it is impossible to calculate the S/N ratios for all the measured 14 roughness parameters. Here in this study, only two parameters Sa and Sdr were chosen to calculate the S/N ratios, because the original Brånemark (commercially pure titanium grade 1) machined implant with a Sa of $0.9 \mu\text{m}$ and an Sdr of 34 % has now been documented with good clinical results for up to 20 years [2]. Therefore in this study, the desired values of parameters $\bar{y}_{Sa} = 0.9 \mu\text{m}$ and $\bar{y}_{Sdr} = 34 \%$ were chosen to be the nominal target.

Subsequently, the ANOVA method was applied to identify the most significant processing factor affecting the surface roughness, the percentage contribution (CP,%) from ANOVA indicating the degree of correlation of a factor. A higher value of CP means the relevant factor is more important for controlling the surface roughness. The analysis procedures and more complete results are detailed in Appendix B.

2.4. Characterization of Ti6Al4V

In order to characterize the microstructure of the Ti6Al4V and obtain a deeper understanding of the formation mechanism of surface morphology, scanning electron microscopy (SEM, FlexSEM1000, with an accelerating voltage of 10/15 kV, employed primarily in secondary electron detection mode) was used to investigate the morphology of the peened surfaces.

Hardness is an important characteristic of biomaterials as it is part of the properties that determine tribological behaviors such as wear resistance or fatigue life. Hardness is affected by the surface topography of the material, thus it would be worthy of understanding how the waterjet influences the hardness distribution along the depth direction, through the generation of plastic deformation and related strain hardening. The Vickers hardness was measured on a microhardness tester (SCTMC HV-1000Z, China). The specimens were cut and embedded, and then, the cross-section of the erosion crater was polished using a metallographic polishing machine for hardness testing. The test force was set at 2.94 N, automatically applied and released with a holding time of 10 s. The hardness value was determined based on the

indentation size by the hardness measuring system. The centerline position of each groove along the movement of the nozzle was measured, and each measuring point was spaced $50 \mu\text{m}$ apart, and the hardness was measured 3–4 times within the same depth. Finally, the average value and standard deviation were calculated.

3. Results

3.1. Surface profile

The 3D topography of the waterjet treated surfaces is shown in Fig. 2. Comparing with the original surface (Fig. 2a), specimens 1, 2, 3 and 6 basically retain the surface texture (Fig. 2(b, c, d, g)); however, the rest of the specimens exhibit the stochastic texture.

Analyzing the evolution of surface height distribution reveals that, for specimens 1 and 2, peak clipping emerges as the primary deformation mechanism, leading to a smoother surface. In contrast, specimens 3 and 6 exhibit substantial plastic deformation due to the sustained impact of the waterjet, resulting in heightened asperities and deeper valleys. With an increase in both kinetic energy and exposure time, material erosion becomes apparent in the remaining specimens, where the emerging surface undergoes a combined effect of peak clipping, valley deepening, and valley filling.

These 3D profiles demonstrate the waviness feature of the treated surface is influenced significantly by the fluid characteristics and reciprocating motion of the waterjet. Therefore, a comprehensive areal surface evaluation including the vertical and horizontal direction is particularly necessary.

3.2. Areal roughness parameters

Table 4 lists the average of three measurements and their standard deviations of 14 surface roughness parameters selected specifically for characterizing the waterjet treated surface. The change rate of each parameter with respect to the untreated specimen is also listed in the table (in brackets). The maximum increase rate is marked in red, on the contrary, all the negative change rates (decrease rate) are colored in green.

The height roughness parameters, Sa and Sq are proportional to the operation pressure. A lower pressure of waterjet would smooth the original surface, taking specimen 1 as an example, the Sa declines almost half. On the contrary, a higher pressure of waterjet would roughen the surface significantly, like specimen 8, the Sa increases more than 3 times. Similarly, the Sp , Sv and Sz values of specimen 1 decrease the most, whereas specimen 8 has the maximum change rates of Sp , Sv and Sz .

Specimen 9 has the highest value of Ssk (pits-dominated), and specimen 1 has the lowest value of Ssk (peaks-dominated). All the Sku values of specimens are lower than 3 except specimens 1 and 3, indicating the height distributions of specimens 1 and 3 are narrower than the Gaussian height distribution.

Sal value has a similar tendency to the Sa . Specimens 1 and 2 have smaller values of Sal than the original specimen indicating that the surfaces are dominated by higher-frequency texture components, while much larger values of Sal of the rest specimens indicate the dominant components have longer wavelengths than the original surface.

All the cases of waterjet treatments are beneficial to increase the Sdr except specimen 1. Specimen 9 has the highest value of Sdr , it increases roughly 2.4 times compared to the original specimen. The only exception is specimen 1 reduced one-third of Sdr . Sdq is a general measurement of the surface slopes and is affected both by height and spacing. The Sdq of a perfectly flat surface is 0, and if the surface is inclined the Sdq will be larger. Specimen 1 was the only one smoothed by the impingement of the waterjet, and the average slopes of the rest specimens all increase, where specimen 9 has the highest slope of the waterjet peened surface.

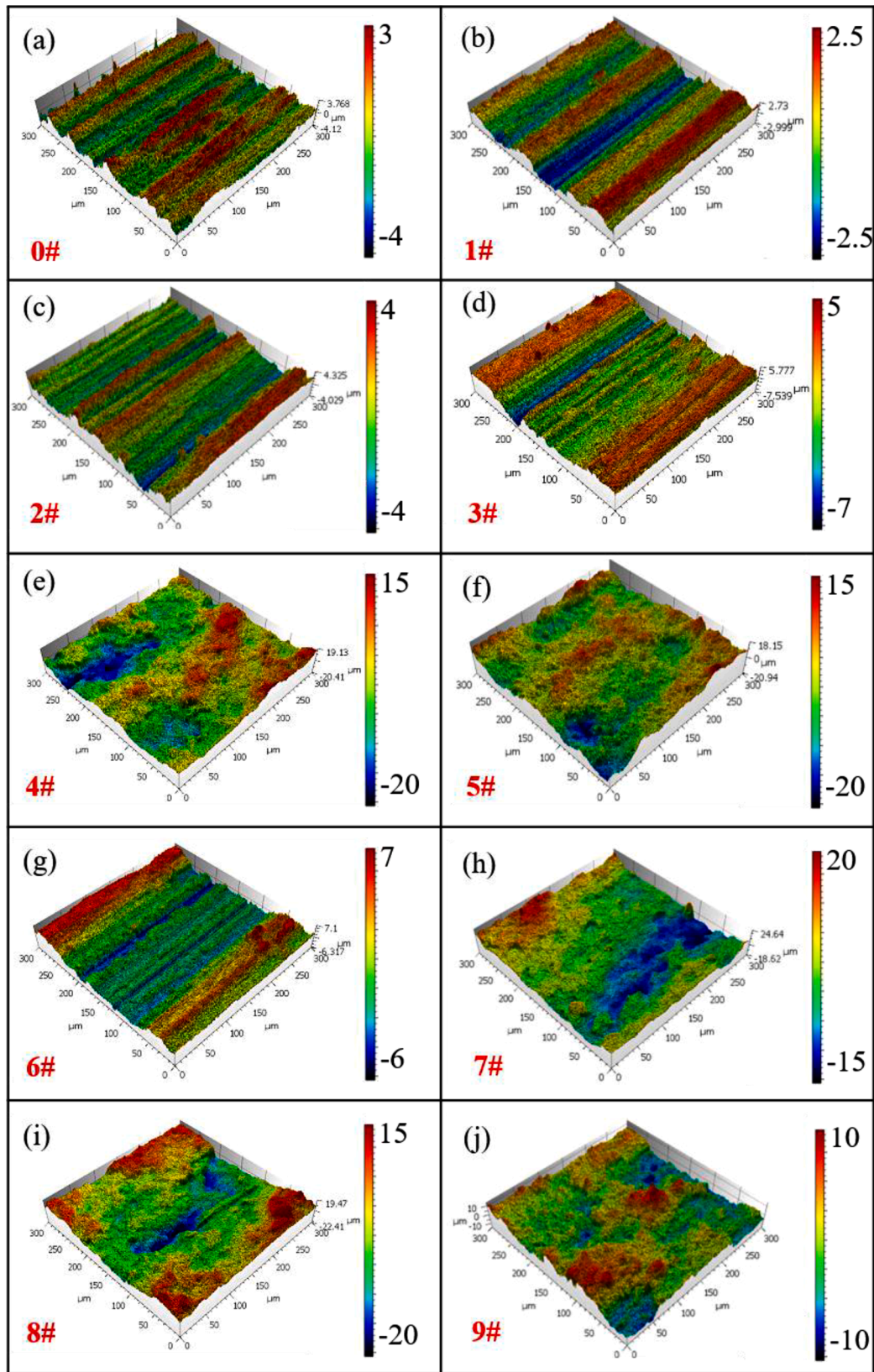


Fig. 2. 3D profiles of (a) untreated surface of Ti6Al4V and (b-j) waterjet treated surfaces under 9 processing conditions (Case 1# - 9#).

Among all the 14 roughness parameters, Spk is the most sensitive parameter to the variation of processing conditions. A large Spk implies a surface composed of high peaks providing a small initial contact area and thus high areas of contact stress when the surface is contacted, for

example, specimen 9. Sk is analogous to Sz , which has a similar but higher change rate than Sz . Svk shows a weak link to the variation of processing conditions that do not have the same trend as any other 13 parameters considered in the study, indicating the waterjet mainly

Table 4
The areal roughness parameters of the untreated and waterjet treated surfaces.

No.	<i>Sa</i> (μm)	<i>Sq</i>	<i>Ssk</i>	<i>Sku</i>	<i>Sp</i> (μm)	<i>Sv</i> (μm)	<i>Sz</i> (μm)
0	1.78 ± 1.17 (0 %)	2.15 ± 1.41 (0 %)	−0.24 ± 0.49 (0 %)	2.31 ± 0.19 (0 %)	5.71 ± 2.78 (0 %)	7.32 ± 5.79 (0 %)	13.03 ± 8.54 (0 %)
1	0.90 ± 0.21 (−49.54 %)	1.16 ± 0.24 (−46.03 %)	−1.01 ± 0.70 (321.79 %)	3.99 ± 1.73 (72.86 %)	2.92 ± 0.81 (−48.88 %)	4.04 ± 1.10 (−44.87 %)	6.96 ± 1.78 (−46.62 %)
2	1.50 ± 0.36 (−15.68 %)	1.83 ± 0.36 (−14.88 %)	−0.28 ± 0.62 (17.29 %)	2.69 ± 0.72 (16.29 %)	7.23 ± 2.51 (26.52 %)	6.37 ± 2.79 (−12.94 %)	13.60 ± 4.93 (4.36 %)
3	2.09 ± 0.25 (17.02 %)	2.64 ± 0.35 (22.80 %)	−0.97 ± 0.30 (305.81 %)	3.84 ± 0.94 (66.26 %)	5.46 ± 1.31 (−4.44 %)	10.64 ± 4.07 (45.29 %)	16.10 ± 4.97 (23.51 %)
4	5.60 ± 0.39 (214.18 %)	6.98 ± 0.49 (224.74 %)	−0.11 ± 0.15 (−55.43 %)	2.78 ± 0.13 (20.51 %)	22.92 ± 4.25 (301.30 %)	21.35 ± 0.93 (191.58 %)	44.27 ± 4.68 (239.66 %)
5	6.37 ± 3.04 (256.94 %)	7.56 ± 3.31 (251.57 %)	−0.11 ± 0.15 (−55.91 %)	2.46 ± 0.60 (6.45 %)	21.47 ± 5.88 (275.85 %)	20.34 ± 5.85 (177.88 %)	41.81 ± 11.21 (220.83 %)
6	2.26 ± 0.20 (26.63 %)	2.70 ± 0.31 (25.34 %)	0.13 ± 0.37 (−152.43 %)	2.18 ± 0.26 (−5.58 %)	7.59 ± 1.77 (32.81 %)	6.89 ± 0.77 (−5.95 %)	14.47 ± 2.48 (11.05 %)
7	5.31 ± 0.48 (197.87 %)	6.54 ± 0.76 (204.03 %)	0.09 ± 0.21 (−138.49 %)	2.54 ± 0.29 (9.74 %)	20.68 ± 3.44 (262.03 %)	17.37 ± 1.73 (137.22 %)	38.04 ± 4.81 (191.91 %)
8	7.20 ± 1.09 (303.44 %)	8.80 ± 1.32 (309.00 %)	−0.34 ± 0.24 (44.33 %)	2.59 ± 0.06 (12.16 %)	22.98 ± 5.53 (302.23 %)	25.91 ± 4.05 (253.87 %)	48.88 ± 9.50 (275.03 %)
9	6.20 ± 3.39 (247.86 %)	7.26 ± 3.37 (237.41 %)	0.20 ± 0.27 (−184.46 %)	2.44 ± 0.90 (5.80 %)	20.78 ± 6.37 (263.77 %)	16.60 ± 3.86 (126.74 %)	37.38 ± 9.77 (186.82 %)

No.	<i>Sal</i> (μm)	<i>Sdr</i> (%)	<i>Sdq</i>	<i>Sk</i> (μm)	<i>Spk</i> (μm)	<i>Svk</i> (μm)	<i>Spc</i>
0	27.84 ± 21.23 (0 %)	18.19 ± 3.22 (0 %)	0.69 ± 0.07 (0 %)	4.20 ± 0.53 (0 %)	0.93 ± 0.08 (0 %)	3.73 ± 4.95 (0 %)	2.22 ± 0.17 (0 %)
1	19.35 ± 9.35 (−30.48 %)	11.70 ± 2.58 (−35.66 %)	0.54 ± 0.06 (−22.44 %)	2.57 ± 0.95 (−38.82 %)	0.33 ± 0.10 (−64.15 %)	2.01 ± 1.28 (−46.08 %)	1.79 ± 0.21 (−19.39 %)
2	21.16 ± 4.44 (−24.00 %)	20.42 ± 2.64 (12.26 %)	0.74 ± 0.05 (6.91 %)	4.28 ± 1.59 (1.91 %)	1.06 ± 0.57 (14.36 %)	2.10 ± 1.18 (−43.62 %)	2.52 ± 0.20 (13.56 %)
3	37.39 ± 15.59 (34.31 %)	21.30 ± 4.37 (17.10 %)	0.78 ± 0.11 (12.80 %)	5.77 ± 1.73 (37.22 %)	0.58 ± 0.28 (−38.09 %)	4.24 ± 0.51 (13.77 %)	2.67 ± 0.05 (20.35 %)
4	48.24 ± 5.00 (73.31 %)	53.50 ± 1.85 (194.17 %)	1.30 ± 0.33 (87.60 %)	17.82 ± 1.34 (324.23 %)	5.57 ± 1.09 (498.63 %)	6.98 ± 0.67 (87.13 %)	2.95 ± 0.11 (32.88 %)
5	41.70 ± 7.31 (49.80 %)	58.93 ± 4.16 (224.05 %)	1.36 ± 0.07 (97.34 %)	21.44 ± 12.14 (410.31 %)	4.52 ± 0.71 (386.06 %)	5.05 ± 0.77 (35.33 %)	3.01 ± 0.16 (35.70 %)
6	32.19 ± 21.19 (15.63 %)	27.64 ± 5.19 (51.98 %)	0.88 ± 0.10 (26.99 %)	6.02 ± 1.68 (43.36 %)	2.54 ± 1.91 (173.35 %)	1.89 ± 1.34 (−49.29 %)	2.85 ± 0.16 (28.46 %)
7	50.84 ± 4.76 (82.64 %)	56.76 ± 1.48 (212.08 %)	1.41 ± 0.00 (104.52 %)	17.37 ± 0.25 (313.44 %)	5.46 ± 2.52 (486.41 %)	4.48 ± 1.66 (20.19 %)	3.99 ± 0.33 (80.07 %)
8	61.12 ± 4.13 (119.58 %)	57.40 ± 2.32 (215.63 %)	1.35 ± 0.04 (94.78 %)	21.72 ± 4.39 (416.90 %)	4.78 ± 1.03 (413.69 %)	9.91 ± 2.27 (165.67 %)	2.80 ± 0.11 (26.05 %)
9	44.81 ± 14.78 (60.96 %)	61.38 ± 8.80 (237.52 %)	1.46 ± 0.11 (111.75 %)	17.67 ± 7.72 (320.50 %)	6.73 ± 2.30 (623.85 %)	3.12 ± 0.83 (−16.25 %)	4.32 ± 0.46 (94.66 %)

The red color represents the maximum increase rate, while the green color stands for the negative change rates.

affects the top and middle parts of the surface profile and has little effect on the surface pits.

Spc has a similar tendency to the two hybrid parameters *Sdr* and *Sdq*, in which specimen 1 and 9 has the minimum and maximum value, respectively. A smaller value indicates that the points of contact with other objects have rounded shapes (specimen 1); a larger value indicates that the points of contact with other objects have pointed shapes (specimen 9).

Looking at the selected 5 sets of 14 parameters, the height parameters provide essentially the same information except the *Ssk* exhibits a distinctive trend. *Sal*, as a spatial parameter, has a similar tendency to the *Sa*. *Sdr* corresponding to the available contact area of implant surface increases in all the cases of waterjet treatments except case 1 (surface smoothing). The three functional parameters (*Spk Sk Svk*) exhibit a more obvious change compared to the *Sp*, *Sv*, and *Sz*. *Spc* and *Sdr* have similarities.

3.3. S/N ratio and ANOVA analysis

The detailed calculation process of S/N ratios can be found in [Appendix A](#). Based on the results, the most significant factor that affects *Sa* is operation pressure, followed by the number of paths and standoff distance. Regarding *Sdr*, operation pressure is also the most significant factor, but standoff distance has a larger influence than the number of paths. [Table 5](#) summarizes the best combination of processing parameters (factor level) for obtaining the desired value of *Sa* = 0.9 μm and an *Sdr* = 34 %. The best waterjet condition is different, which yields a

Table 5
The best combination of factor levels for obtaining the desired roughness values.

Factor	<i>Sa</i>	<i>Sdr</i>
<i>Pw</i> (MPa)	100 (level 1)	200 (level 2)
SOD (mm)	50 (level 1)	150 (level 3)
<i>n</i>	2 (level 1)	2 (level 1)

tradeoff problem when using waterjet to obtain a desired surface.

The percentage of contributions for all factors is shown in [Table 6](#), and the corresponding ANOVA analysis results (degree of freedom, sum of squares, values of variance, F-ratio, *p*-value) are listed in [Appendix B](#). These results show that the operation pressure *Pw* is the most influential parameter to the 14 roughness parameters, especially contributing to the change of *Spk* the most by 85.07 %. The *p*-value of *Spk* is 0.028, which is less than 0.05.

For the most height parameters (*Sa Sq Sku Sv Sz*) and *Sk*, the operating pressure was the most significant factor in controlling the surface profile, followed by the standoff distance and the number of jet passes. However, the number of waterjet path plays a more important role in controlling the spatial (*Sal*), hybrid (*Sdr* and *Sdq*), functional (*Spk*) and feature (*Spc*) parameters compared to the standoff distance.

There is only one exception, namely *Svk*. All three factors have small effects on *Svk*, and the number of waterjet path contributes less than 1 %. This can be explained by the fact that the majority of the kinetic energy of the waterjet transfers to the change of surface peak and core

Table 6

The percentage of contributions to the 14 parameters for all factors.

Parameters	Pw (%)	SOD (%)	n (%)	Parameters	Pw (%)	SOD (%)	n (%)
Sa	74.53	7.67	4.82	Sal	69.20	1.03	4.04
Sq	73.75	7.82	4.69	Sdr	80.73	3.59	10.60
Ssk	66.45	1.73	12.15	Sdq	82.21	1.86	12.85
Sku	62.86	12.71	5.46	Sk	70.41	10.87	7.08
Sp	73.34	9.61	9.77	Spk	85.07	0.84	11.64
Sv	56.33	12.09	4.82	Svk	25.18	18.06	1.00
Sz	66.98	10.87	6.95	Spc	62.20	8.89	25.44
				Spk + Sk + Svk	70.62	9.87	4.66

height and leaves no more sufficient energy to cause a notable change in the valley part. Alternatively, the functional surface height ($Spk + Sk + Svk$) as a single parameter is considered and the contribution percentage of each parameter is calculated. It is found that operation pressure contributes the most by 70.62 %, and this is followed by standoff distance at 9.87 % and the number of waterjet path at 4.66 %.

3.4. SEM analysis

The surface morphology of the original and treated specimens is shown in Fig. 3. In general, the impact of waterjet makes the surface rougher, and higher pressure of waterjet causes the material removal (Fig. 3(e, f, h, i, j)), and a longer standoff distance widens the groove generated by the waterjet impingement (Fig. 3e vs. 3f, Fig. 3i vs. 3j), but the influence of multiple passes is less significant compared to the pressure and the standoff distance.

The process of waterjet impacts is highly stochastic in nature. This can be seen from Fig. 3(e, f) of cases 4 and 5 where the impacting waterjet has not fully covered the surface by leaving some areas of the original surface. However, with higher operation pressure although at a longer standoff distance, the whole surface was covered by the impacting waterjet with indents as shown in Fig. 3(h, i, j). This indicates that the surface has been repeatedly impacted by the water droplets with higher kinetic energy during multiple jet passes thus leaving no more of the original surface.

Based on the height distribution evolution, it can be seen that by tuning the waterjet processing parameters, mainly the factor operation pressure, the waterjet can either smooth (cases 1# and 2#) or roughen (cases 3# and 6#) or erode (cases 4#, 5#, 7#, 8# and 9#) the surface. When the kinetic energy of the waterjet is not sufficient, the specimens remain as a striated surface, with only a slight change in the amplitude and waviness (case 1#, 2#, 3# and 6#). However, when the energy is increased and the surface material is completely eroded, the randomness of the waterjet-peened specimen can be observed. With probability distribution of droplet size and velocity, the waterjet creates a random surface that is different from the initial engineering surface.

Fig. 4 shows the detailed waterjet eroded surface with random-distributed pores. The impacting process in the waterjet treatment is somehow similar to the shot peening using small solid balls [57], thus it can remove the material with sufficiently high pressure of waterjet. The presence of pores on the surface is not necessarily negative, as it may enhance osteointegration by increasing the contact area between the implant and the surrounding bone tissue [58].

As Fig. 5 displays, when the pressure is up to 300 MPa, waterjet forms grooves of different depths on the surface at a different standoff distance. Because a shorter standoff distance brings more kinetic energy to the waterjet, the groove is deeper compared to the other two cases.

It should be admitted that the original surface of the specimen was not polished to a finer texture but tried to keep the machined coarse surface as Figs. 2(a) and 3(a) show, as occurs in commercial machined implants. During future experiments, the Ti6Al4V surface should be first ground with SiC papers and polished with diamond abrasive cloth plus some finer polishing methods and then perform waterjet processing.

3.5. Surface hardness

According to Fig. 2, the top surface layers of specimens 4, 5, 7, 8 and 9 have been removed and revealed the stochastic nature of the waterjet treated surface, so we tested the surface hardness along the depth direction of these five specimens. The Vickers hardness result is shown in Fig. 6. The obtained profile was characterized by a hardened layer of thickness 300 ~ 400 μm . Specimen 7 exhibits the highest value of hardness, which increases by roughly 21.11 % compared to the value of the unhardened layer. Specimen 5, on the contrary, possesses the lowest value of hardness, which only increases by 6.76 %. Note that the peak value of hardness did not appear at the top layer but at a certain distance beneath the top surface. For example, the peak hardness of specimen 7 is located at a depth of around 70 μm .

The main reason that the peak hardness was observed below the surface is the influence of residual stresses. The impingements of the waterjet generate compressive residual stresses in the material due to the peening effect. It was found that the hardness increases with compressive residual stress, whilst it decreases with tensile residual stress [58,59]. A secondary reason could be the material erosion on the top surface that weakens the hardness at the top surface [29]. The last but not least explanation could be the Hertz theory. What is good for elastic contact can be extended beyond yield regarding the depth at which hardness is peaking [60]. As a result of these factors, the peak hardness value was found below the surface layer.

4. Discussion

When evaluating biomaterial surface topography, Sa stands out for its simplicity, making it a preferred choice. Notably, Ssk in the height category exhibits a distinct trend, emphasizing its relevance. Additionally, Sal , as a spatial parameter, is recommended for inclusion in the analysis, and Sdr , with clear biological significance, is strongly advised for assessment. The three functional parameters Sk , Spk and Svk , directly impacting bearing capacity, are invaluable additions to the analysis. In summary, prioritizing Sa , Ssk , Sal , and Sdr is advisable, with Sk , Spk , and Svk serving as supplementary parameters.

Based on the S/N ratio and ANOVA analysis, it becomes evident that the pivotal factor in governing surface characteristics is the operating pressure. Furthermore, fine-tuning surface height can be achieved by adjusting the standoff distance, while refining surface waviness can be accomplished through the manipulation of the number of cutting paths. Moreover, an additional challenge lies in the creation of a hierarchical surface structure using the waterjet method. This may necessitate the integration of waterjet technology with other approaches, such as laser shock peening, to simultaneously generate hierarchical surfaces.

Waterjet treatment at room temperature prevents thermal oxidation, ensuring the hardened layer matches the original specimen. Any potential oxidation is minimal, as seen in laser shock peening on Ti6Al4V, producing a mere 5 μm layer [61]. Plastic deformation alone can yield a thicker hardened layer, extending to a few hundred microns [29,62]. EBSD results for specimen 4 (Fig. C.1 in Appendix C) show small crystal size, with black areas indicating substantial residual stresses. Waterjet impingements induce compressive residual stresses, the main driver of

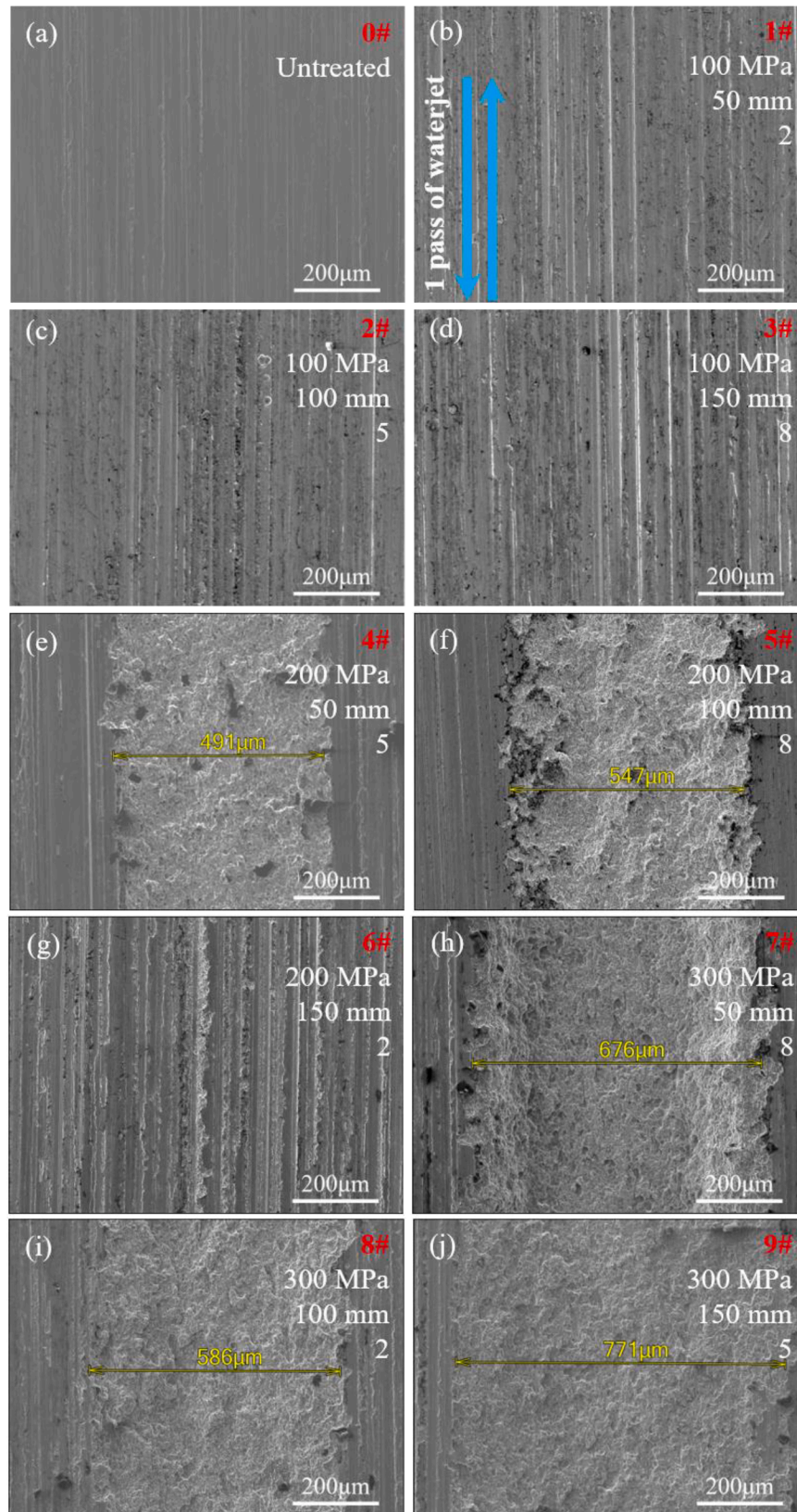


Fig. 3. SEM images of untreated and treated surfaces of Ti6Al4V.

the hardened layer, as hardness correlates with these stresses [58,59].

The current study focuses on surface roughness at the micron scale, with minimal consideration of nanoscale parameters. Generating a surface with a nanopattern has become popular [3,17] because the

nanoscale roughness affects the fast regeneration of the fibrous soft tissue after implantation [18,19]. To assess the waterjet-treated surface at the nanoscale, atomic force microscopy (AFM) was employed. Regrettably, the results (Fig. D.1 in Appendix D) did not align with

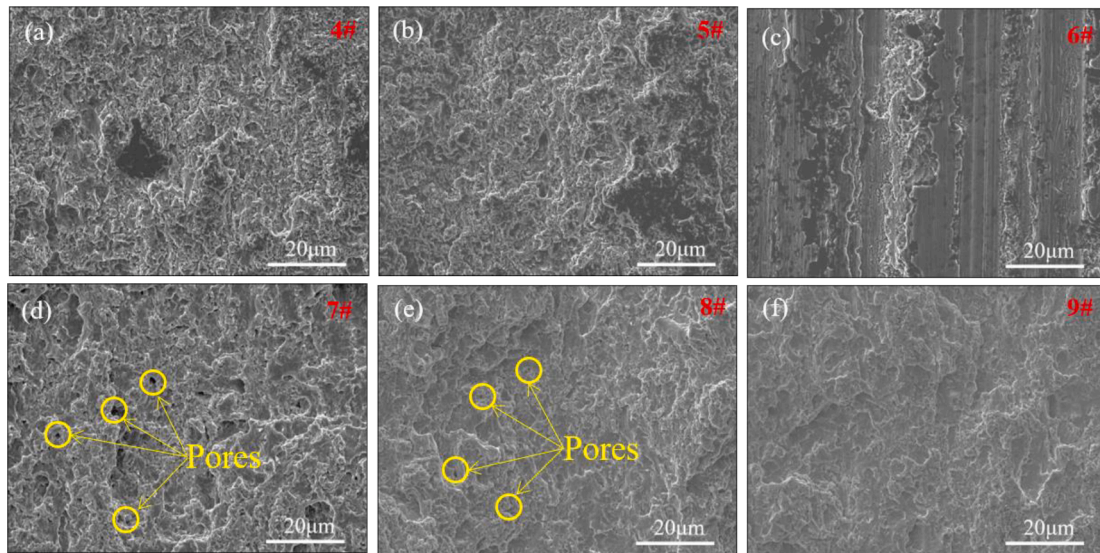


Fig. 4. SEM images of damaged Ti6Al4V surfaces induced by the waterjet impact at different processing conditions (Case 4# - 9#).

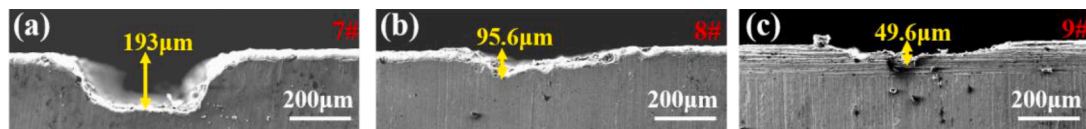


Fig. 5. Cross-section views of specimens treated at different processing conditions (Case 7# - 9#).

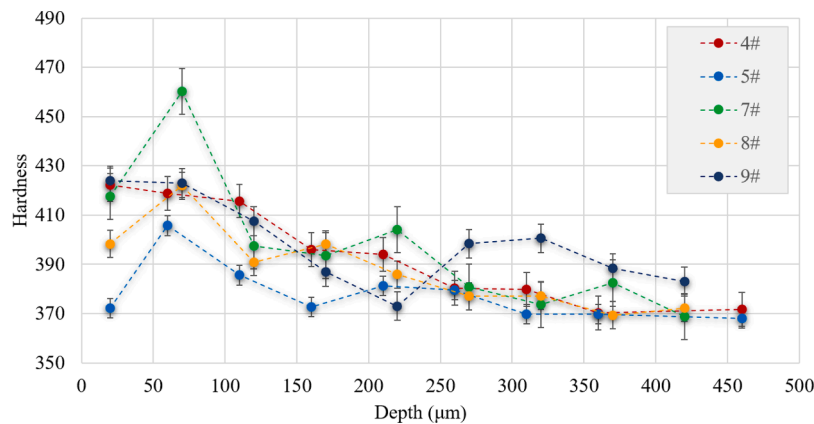


Fig. 6. The Vickers hardness results along the depth of different specimens.

expectations, as significant nanopatterns were not observed, and a majority of the specimens were not suitable for AFM examination. This outcome may be attributed to limitations in waterjet atomization at the nanoscale, influenced by surface tension. Even if nanoscale droplets were present, their kinetic energy decreased significantly due to multiple fragmentations [63], rendering it insufficient to modify surface morphology. Achieving precise control over surface morphology is intrinsically linked to the waterjet atomization process, warranting further theoretical and experimental investigations to enhance control accuracy.

The most fundamental starting point of biomaterial surface control is to determine what kind of surface morphology (S_a and S_{dr}) is most beneficial to improve the biocompatibility and long-term stability of the implant (hardness distribution along the depth direction), then use the most effective surface treatment method (waterjet) to generate the desired surface. This study provides the tools needed to achieve them.

5. Conclusion

Using the Taguchi method, nine waterjet experimental cases were designed and conducted. The influence of the operation pressure, standoff distance, and the number of paths on the surface topography and the areal roughness parameters as well as the hardness were analyzed and discussed. The main conclusion is drawn as follows:

- Among the three process parameters of waterjet treatment, the most critical one is the operation pressure. The standoff distance is beneficial for finer control of the height parameters, whilst the number of paths affects the waviness.
- By increasing the operation pressure from 100 to 300 MPa, the surface of Ti6Al4V specimens can be smoothed, roughened, or damaged; when the surface layer is eroded, the new-born surface exhibits a clear stochastic nature accompanied by microvoids.

- The hardening effect generated by the impingement of waterjet spans over a few hundred microns width, with the peak microhardness being found at a depth of 70 μm , which increases by over 20 %.
- After a comprehensive analysis of the 5 categories of 14 areal roughness parameters, the parameters of Sa , Ssk , Sal , and Sdr as a set are recommended to characterize the biomaterial's surface.

Declaration of Competing Interest

The authors declare that they have no known competing financial

interests or personal relationships that could have appeared to influence the work reported in this paper.

Acknowledgments

The authors appreciate the financial support from the National Nature Science Foundation of China (NSFC, No. 12002052 and No. 12272053). QX and YQ would like to acknowledge the support from the Li Ka Shing Foundation (Grant No: O2022002).

Appendix A. Taguchi method

The experimental design by using the Taguchi method is to identify the best set of processing parameters among the effective factors with a reduced number of experiments. The major steps are as follows:

- (1) Factors selection;
- (2) Selection of orthogonal array and factor levels;
- (3) Conduct experiments described by trials in orthogonal arrays;
- (4) Analyze and interpret the results of the experimental trials.

A.1. Factor selection

In this study, the factors taken into consideration are operation pressure (F1), standoff distance (F2) and the number of paths (F3).

A.2. Orthogonal array

Because three factors are selected with 3 different values (3 levels), a suitable L9 (3^3) orthogonal array is designated as illustrated in [Table 2](#).

A.3. Experiments

The pure waterjet tests were conducted according to the sets of control factors obtained from the L9 orthogonal array, and the measured values of Sa and Sdr are listed in [Table 4](#).

A.4. Results analysis

There are 3 types of S/N ratios depending on the desired performance response:

- The larger the better (for making the system response as large as possible):

$$\left(\frac{S}{N}\right)_L = -10\log\left(\frac{1}{k} \sum_{i=1}^k \frac{1}{y_i^2}\right)$$

- The smaller the better (for making the system response as small as possible):

$$\left(\frac{S}{N}\right)_s = -10\log\left(\frac{1}{k} \sum_{i=1}^k y_i^2\right)$$

- Nominal the best (for reducing variability around a target):

$$\left(\frac{S}{N}\right)_T = 10\log\left(\frac{\bar{y}^2}{\sigma^2}\right)$$

where $\bar{y} = \frac{1}{k} \sum_{i=1}^k y_i$, and $\sigma = \sqrt{\sum_{i=1}^k \frac{(y_i - \bar{y})^2}{k-1}}$, k is the number of measurements in an orthogonal array row and y_i is the measured value in a row.

Nominal the best (S/N)_T was used in this study. For row 1#, $k = 3$ and $y_1 = 1.06$, $y_2 = 0.98$, $y_3 = 0.67$, and therefore,

$$\begin{aligned}
\left(\frac{S}{N}\right)_{Sa} &= 10\log\left(\frac{y_{Sa}^2}{\sum_{i=1}^3 \frac{(y_i - y_{Sa})^2}{3-1}}\right) \\
&= 10\log\left[\frac{0.9^2}{\frac{(1.06-0.9)^2}{2} + \frac{(0.98-0.9)^2}{2} + \frac{(0.67-0.9)^2}{2}}\right] \\
&= 12.81 \\
\left(\frac{S}{N}\right)_{Sdr} &= 10\log\left(\frac{y_{Sdr}^2}{\sum_{i=1}^3 \frac{(y_i - y_{Sdr})^2}{3-1}}\right) \\
&= 10\log\left[\frac{34^2}{\frac{(9.74-34)^2}{2} + \frac{(14.62-34)^2}{2} + \frac{(10.74-34)^2}{2}}\right] \\
&= 1.86
\end{aligned}$$

Similarly, the S/N ratio for other rows is obtained and shown in Table A.1.

Table A.1
L9 orthogonal array and experiment design.

Case No.	Sa (μm)	S/N Ratio	Sdr (%)	S/N Ratio
1#	0.90	12.81	11.70	1.86
2#	1.50	0.78	20.42	6.10
3#	2.09	-4.29	21.30	6.46
4#	5.60	-16.15	53.50	3.04
5#	6.37	-18.24	58.93	0.85
6#	2.26	-5.40	27.64	11.21
7#	5.31	-15.61	56.76	1.71
8#	7.20	-18.74	57.40	1.45
9#	6.20	-18.22	61.38	-0.17

The S/N ratio of Sa for the level 1 of operation pressure (100 MPa) is obtained as follows:

$$level1 = \frac{(12.81 + 0.78 - 4.29)}{3} = 3.10$$

Similarly, the average S/N ratio for each level of each factor is obtained and shown in Table A.2. From the S/N ratio response, the best combination of parameters can be identified by selecting the highest value from each factor, as summarized in Table 5.

Table A.2
Response of S/N ratio for each level of each factor.

Level	Sa			Sdr		
	Pw	SOD	n	Pw	SOD	n
1	3.10	-6.31	-3.78	4.81	2.21	4.84
2	-13.26	-12.07	-11.19	5.03	2.80	2.99
3	-17.52	-9.30	-12.71	1.00	5.83	3.01
Max. Difference	20.62	5.76	8.93	4.03	3.62	1.85

Appendix B. Analysis of Variance (ANOVA)

First of all calculate the degree of freedom for all factors. The total degree of freedom (DF) is

$$DF_T = N - 1 = 9 - 1 = 8$$

where N is the number of cases.

For factor A (operation pressure) $DF_A = k_A - 1 = 3 - 1 = 2$, similarly $DF_B = DF_C = 2$. For error, $DF_e = DF_T - (DF_A + DF_B + DF_C) = 2$.

According to Table 4, the total sum of squares (SS) of Sa is

$$\begin{aligned}
 SS_T &= \sum_{i=1}^N y_i^2 - \frac{\left(\sum_{i=1}^N y_i\right)^2}{N} \\
 &= (0.90^2 + 1.50^2 + \dots + 6.20^2) - \frac{(0.90 + 1.50 + \dots + 6.20)^2}{9} \\
 &= 47.27
 \end{aligned}$$

Factor A that has 3 levels

$$\begin{aligned}
 SS_A &= \left[\frac{\left(\sum y_{A1}\right)^2}{k_{A1}} + \frac{\left(\sum y_{A2}\right)^2}{k_{A2}} + \frac{\left(\sum y_{A3}\right)^2}{k_{A3}} \right] - \frac{\left(\sum y_i\right)^2}{N} \\
 &= \frac{(0.90 + 1.50 + 2.09)^2}{3} + \dots - \frac{(0.90 + 1.50 + \dots + 6.20)^2}{9} \\
 &= 35.25
 \end{aligned}$$

Similarly, $SS_B = 3.62$, $SS_C = 2.29$. For error $SS_e = SS_T - (SS_A + SS_B + SS_C) = 6.12$.

Then the value of variance (VV) for factor A

$$VV_A = \frac{SS_A}{DF_A} = 17.62$$

Similarly, $VV_B = 1.81$, $VV_C = 1.14$, and for error $VV_e = (SS_e / DF_e) = 3.06$.

After this, the F-ratio for all factors are calculated as follows:

$$F_A = \frac{VV_A}{VV_e} = \frac{17.62}{3.06} = 5.76$$

Similarly, $F_B = (VV_B / VV_e) = 0.59$ and $F_C = (VV_C / VV_e) = 0.37$.

At the last, the percentage contribution (CP, %) for all factors is calculated as shown below:

$$CP_A = \frac{SS_A}{SS_T} \times 100\% = 74.53\%$$

Similarly, $CP_B = (SS_B / SS_T) \times 100\% = 7.67\%$, $CP_C = (SS_C / SS_T) \times 100\% = 4.82\%$.

The result of ANOVA analysis is presented in Table B.1, B.2 and B.3. Degree of freedom is the number of levels of a factor minus 1, and the sum of squares indicates the total amount of dispersion within levels, values of variance express dispersion (or, how far the data are scattered from the mean), and F-ratio represents the variation of a factor. The F-ratio is simply a ratio of factor to error variance. The p -value of the F statistic shows how likely it is that the F-ratio calculated from the test would have occurred if the null hypothesis of no difference among group means were true.

Table B.1
The ANOVA analysis results for the factor of operation pressure.

Roughness	DF	SS	VV	F-ratio	p -value
<i>Sa</i>	2	35.24	17.62	5.74	0.148
<i>Sq</i>	2	50.17	25.08	5.37	0.157
<i>Ssk</i>	2	1.07	0.53	3.38	0.228
<i>Sku</i>	2	2.04	1.02	3.31	0.232
<i>Sp</i>	2	429.16	214.58	10.08	0.090
<i>Sv</i>	2	265.93	132.96	2.10	0.323
<i>Sz</i>	2	1369.60	684.82	4.41	0.185
<i>Sal</i>	2	1041.90	520.93	2.69	0.271
<i>Sdq</i>	2	0.81	0.41	26.73	0.036
<i>Sdr</i>	2	2631.10	1315.50	15.90	0.059
<i>Sk</i>	2	349.65	174.82	6.04	0.142
<i>Spk</i>	2	39.72	19.86	34.81	0.028
<i>Svk</i>	2	14.20	7.10	0.45	0.690
<i>Spc</i>	2	2.86	1.43	17.95	0.053

A small p -value (<0.05) indicates that the difference between group means is statistically significant, in other words, the processing parameter has a significant influence on the test results. As Table B.1 shows, *Sdq* and *Spk* are influenced by the change of operation pressure most. However, a large p -value (>0.95) indicates that the null hypothesis is true, and there is no difference between group means. Based on Tables B.2 and B.3 results, *Sal* is not affected by the standoff distance and the number of the path has no effects on the *Svk*.

Table B.2

The ANOVA analysis results for the factor of standoff distance.

Roughness	DF	SS	VV	F-ratio	p-value
<i>Sa</i>	2	3.63	1.81	0.59	0.629
<i>Sq</i>	2	5.32	2.66	0.57	0.637
<i>Ssk</i>	2	0.03	0.01	0.09	0.917
<i>Sku</i>	2	0.41	0.21	0.67	0.599
<i>Sp</i>	2	56.25	28.13	1.32	0.431
<i>Sv</i>	2	57.06	28.53	0.45	0.690
<i>Sz</i>	2	222.30	111.15	0.72	0.581
<i>Sal</i>	2	15.45	7.73	0.04	0.962
<i>Sdq</i>	2	0.02	0.01	0.61	0.621
<i>Sdr</i>	2	116.98	58.49	0.71	0.585
<i>Sk</i>	2	53.99	26.99	0.93	0.518
<i>Spk</i>	2	0.39	0.20	0.34	0.746
<i>Svk</i>	2	10.19	5.09	0.32	0.758
<i>Spc</i>	2	0.41	0.20	2.57	0.280

Table B.3

The ANOVA analysis results for the factor of the number of path.

Roughness	DF	SS	VV	F-ratio	p-value
<i>Sa</i>	2	2.28	1.14	0.37	0.730
<i>Sq</i>	2	3.19	1.60	0.34	0.746
<i>Ssk</i>	2	0.19	0.10	0.62	0.617
<i>Sku</i>	2	0.18	0.09	0.29	0.775
<i>Sp</i>	2	57.17	28.59	1.34	0.427
<i>Sv</i>	2	22.74	11.37	0.18	0.847
<i>Sz</i>	2	142.21	71.11	0.46	0.685
<i>Sal</i>	2	60.86	30.43	0.16	0.862
<i>Sdq</i>	2	0.13	0.06	4.18	0.193
<i>Sdr</i>	2	345.53	172.77	2.09	0.324
<i>Sk</i>	2	35.14	17.57	0.61	0.621
<i>Spk</i>	2	5.43	2.72	4.76	0.174
<i>Svk</i>	2	0.56	0.28	0.02	0.980
<i>Spc</i>	2	1.17	0.58	7.34	0.120

Appendix C. Electron backscatter diffraction characterization

Electron backscatter diffraction (EBSD) measurements were carried out to analyze the microstructure of the waterjet treated sample's cross-section (specimen 4). The working distance, current, and voltage were set to be 15 mm, 10 nA, and 20 keV, respectively. The characterization was performed on Zeiss Gemini 450 with an Oxford EBSD detector.

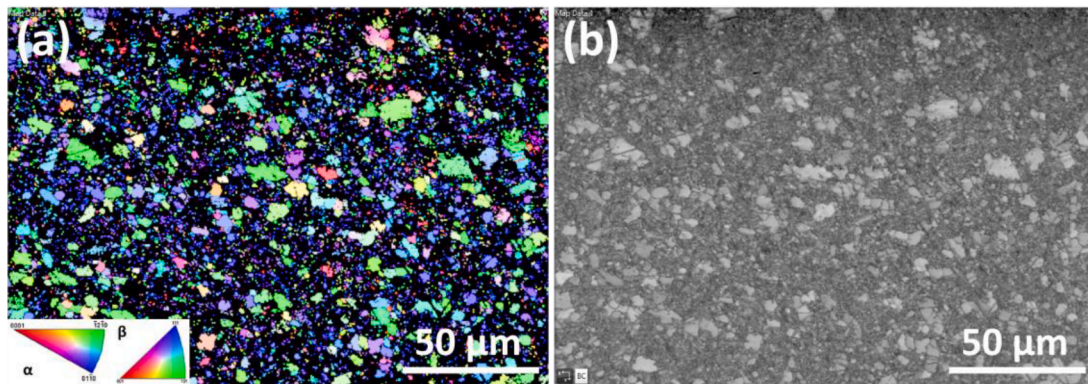


Fig. C.1. (a) Inverse pole figure image and (b) the corresponding band contrast image of the cross-section area of waterjet treated specimen 4.

Appendix D. Atomic force microscope characterization

Atomic force microscopy (AFM, Bruker Dimension XR FastScan) analysis was used to observe the nanoscale feature of the waterjet treated surface. The AFM scanning was performed in tapping mode with a scanning frequency of 0.498 Hz and a scan length of 50 μm. The results (Fig. C.1) indicate that the surface modification at the nanoscale is quite limited. Moreover, the specimens from case 4 to case 9 failed in the AFM analysis because the surface height difference was too large to be measured by the AFM.

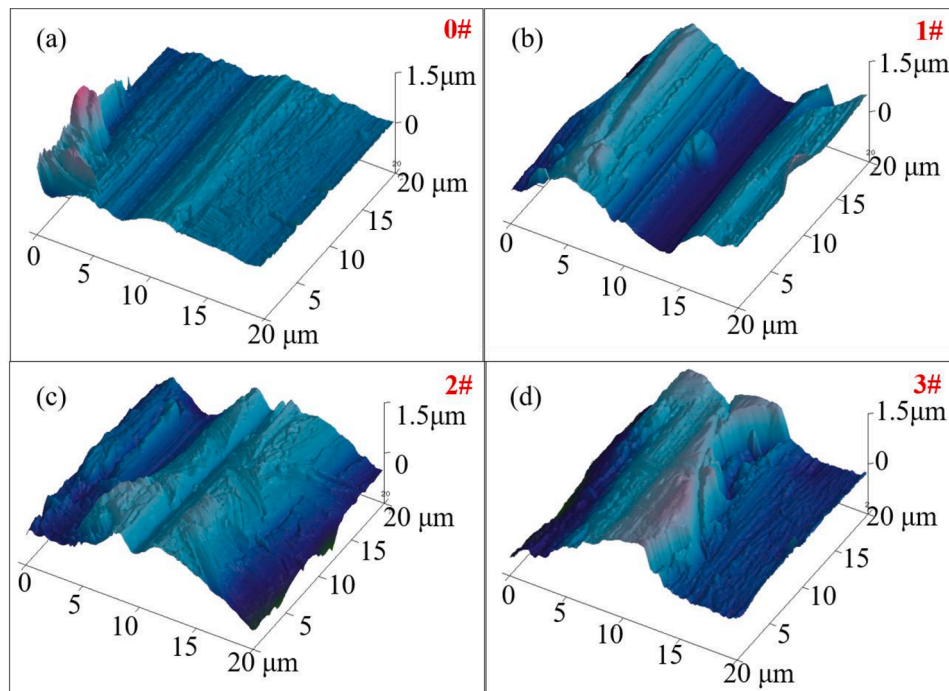


Fig. D.1. AFM images of (a) original engineering surface of Ti6Al4V and (b-d) waterjet treated surfaces under 3 processing conditions (Case 1# - 3#).

References

- [1] D. Khang, J. Lu, C. Yao, K.M. Haberstroh, T.J. Webster, The role of nanometer and sub-micron surface features on vascular and bone cell adhesion on titanium, *Biomaterials* 29 (2008) 970–983, <https://doi.org/10.1016/j.biomaterials.2007.11.009>.
- [2] A. Wennerberg, T. Albrektsson, On implant surfaces: a review of current knowledge and opinions, *Int. J. Oral Maxillofac. Implants.* 25 (2009) 63–74, <https://doi.org/10.1111/j.1600-051X.2008.01321.x>.
- [3] L. Le Guéhennec, A. Soueidan, P. Layrolle, Y. Amouriq, Surface treatments of titanium dental implants for rapid osseointegration, *Dent. Mater.* 23 (2007) 844–854, <https://doi.org/10.1016/j.dental.2006.06.025>.
- [4] C. Larsson, P. Thomsen, B.O. Aronsson, M. Rodahl, J. Lausmaa, B. Kasemo, L. E. Ericson, Bone response to surface-modified titanium implants: studies on the early tissue response to machined and electropolished implants with different oxide thicknesses, *Biomaterials* 17 (1996) 605–616, [https://doi.org/10.1016/0142-9612\(96\)88711-4](https://doi.org/10.1016/0142-9612(96)88711-4).
- [5] K. Shemtov-Yona, D. Rittel, Fatigue of dental implants: facts and fallacies, *Dent. J.* 4 (2016) 16, <https://doi.org/10.1016/j.dental.2016.06.025>.
- [6] D. Karazisis, L. Rasmussen, S. Petronis, A. Palmquist, F.A. Shah, H. Agheli, L. Emanuelsson, A. Johansson, O. Omar, P. Thomsen, The effects of controlled nanotopography, machined topography and their combination on molecular activities, bone formation and biomechanical stability during osseointegration, *Acta Biomater.* 136 (2021) 279–290, <https://doi.org/10.1016/j.actbio.2021.10.001>.
- [7] S. Barriuso, M. Lieblich, M. Multigner, I. Etcheberria, A. Alberdi, J.L. González-Carrasco, Roughening of metallic biomaterials by abrasiveless waterjet peening: characterization and viability, *Wear* 270 (2011) 634–639, <https://doi.org/10.1016/j.wear.2011.01.024>.
- [8] D. Klichova, A. Nag, J. Poloprudský, J. Foldyna, F. Pude, L. Sitek, S. Hloch, Utilising of water hammer effect for surface roughening of Ti6Al4V, *Int. J. Adv. Manuf. Technol.* 126 (2023) 5633–5647, <https://doi.org/10.1007/s00170-023-11521-y>.
- [9] S. Qutaba, M. Asmelash, K. Saptaji, A. Azhari, A Review On Peening Processes and Its Effect On Surfaces, Springer, London, 2022, <https://doi.org/10.1007/s00170-022-09021-6>.
- [10] J. Folkes, Waterjet—An innovative tool for manufacturing, *J. Mater. Process. Technol.* 209 (2009) 6181–6189, <https://doi.org/10.1016/j.jmatprotec.2009.05.025>.
- [11] M. Lieblich, S. Barriuso, J. Ibáñez, L. Ruiz-de-Lara, M. Díaz, J.L. Ocaña, A. Alberdi, J.L. González-Carrasco, On the fatigue behavior of medical Ti6Al4V roughened by grit blasting and abrasiveless waterjet peening, *J. Mech. Behav. Biomed. Mater.* 63 (2016) 390–398, <https://doi.org/10.1016/j.jmbbm.2016.07.011>.
- [12] T.A. Taylor, Surface roughening of metallic substrates by high pressure pure waterjet, *Surf. Coat. Technol.* 76–77 (1995) 95–100, [https://doi.org/10.1016/0257-8972\(95\)02528-6](https://doi.org/10.1016/0257-8972(95)02528-6).
- [13] D. Arola, L. McCain, Abrasive waterjet peening: a new method of surface preparation for metal orthopedic implants, *J. Biomed. Mater. Res. (Appl. Biomater.)* 53 (2000) 536–546.
- [14] J. Xie, D. Rittel, A two-dimensional model for metallic surface roughness resulting from pure waterjet peening, *Int. J. Eng. Sci.* 120 (2017) 189–198, <https://doi.org/10.1016/j.ijengsci.2017.08.010>.
- [15] J. Xie, D. Rittel, Three-dimensional stochastic modeling of metallic surface roughness resulting from pure waterjet peening, *Int. J. Eng. Sci.* 120 (2017) 241–253, <https://doi.org/10.1016/j.ijengsci.2017.08.011>.
- [16] J. Xie, D. Rittel, The effects of waterjet peening on a random-topography metallic implant surface, *Eur. J. Mech. - A/Solids* 71 (2018) 235–244, <https://doi.org/10.1016/j.euromechsol.2018.03.022>.
- [17] J. Xie, D. Rittel, P. Chen, Modeling the topographic evolution of a rough metallic surface resulting from impact of water droplets, *Int. J. Eng. Sci.* 144 (2019), 103142, <https://doi.org/10.1016/j.ijengsci.2019.103142>.
- [18] J. Xie, P. Chen, D. Rittel, Finite element modeling of multiple water droplets impact onto a rough surface: Re-assessing Sa and surface wavelength, *J. Mech. Behav. Biomed. Mater.* 110 (2020), 103816, <https://doi.org/10.1016/j.jmbbm.2020.103816>.
- [19] D. Arola, M.L. McCain, S. Kunaporn, M. Ramulu, Waterjet and abrasive waterjet surface treatment of titanium: a comparison of surface texture and residual stress, *Wear* 249 (2001) 943–950, [https://doi.org/10.1016/S0043-1648\(01\)00826-2](https://doi.org/10.1016/S0043-1648(01)00826-2).
- [20] S. Kunaporn, M. Hashish, Waterjet machining and peening, *Analyzer* 122 (2000) 90–95, <https://doi.org/10.1115/1.556155>.
- [21] A. Chillman, M. Ramulu, M. Hashish, Waterjet peening and surface preparation at 600 MPa: a preliminary experimental study, *J. Fluids Eng.* 129 (2007) 485, <https://doi.org/10.1115/1.2436580>.
- [22] A. Chillman, M. Ramulu, M. Hashish, Waterjet and water-air jet surface processing of a titanium alloy: a parametric evaluation, *J. Manuf. Sci. Eng.* 132 (2010) 11012, <https://doi.org/10.1115/1.4000837>.
- [23] L. Huang, P. Kinnell, P.H. Shipway, Removal of heat-formed coating from a titanium alloy using high pressure waterjet: influence of machining parameters on surface texture and residual stress, *J. Mater. Process. Technol.* 223 (2015) 129–138, <https://doi.org/10.1016/j.jmatprotec.2015.03.053>.
- [24] A. Azhari, C. Schindler, E. Kersch, P. Grad, Improving surface hardness of austenitic stainless steel using waterjet peening process, *Int. J. Adv. Manuf. Technol.* 63 (2012) 1035–1046, <https://doi.org/10.1007/s00170-012-3962-1>.
- [25] A. Azhari, C. Schindler, K. Hilbert, C. Godard, E. Kersch, Influence of waterjet peening and smoothing on the material surface and properties of stainless steel 304, *Surf. Coatings Technol.* 258 (2014) 1176–1182, <https://doi.org/10.1016/j.surfcoat.2014.07.013>.
- [26] A. Azhari, C. Schindler, C. Godard, J. Gibmeier, E. Kersch, Effect of multiple passes treatment in waterjet peening on fatigue performance, *Appl. Surf. Sci.* 388 (2016) 468–474, <https://doi.org/10.1016/j.apsusc.2015.11.195>.
- [27] S. Kunaporn, A. Chillman, M. Ramulu, M. Hashish, Effect of waterjet formation on surface preparation and profiling of aluminum alloy, *Wear* 265 (2008) 176–185, <https://doi.org/10.1016/j.wear.2007.09.008>.

- [28] F. Boud, L.F. Loo, P.K. Kinnell, The impact of plain waterjet machining on the surface integrity of aluminium 7475, *Procedia CIRP* 13 (2014) 382–386, <https://doi.org/10.1016/j.procir.2014.04.065>.
- [29] A. Azhari, C. Schindler, B. Li, Effect of waterjet peening on aluminum alloy 5005, *Int. J. Adv. Manuf. Technol.* 67 (2013) 785–795, <https://doi.org/10.1007/s00170-012-4522-4>.
- [30] X. Ding, Y. Kang, D. Li, X. Wang, D. Zeng, Experimental investigation on surface quality processed by self-excited oscillation pulsed waterjet peening, *Materials (Basel)* 10 (2017), <https://doi.org/10.3390/ma10090989>.
- [31] M.Y. Amegadzie, E.D. Moreau, B. Christensen, I.W. Donaldson, A. Tieu, K. P. Plucknett, The impact of sintered density upon the microstructural and residual stress development in an ultrasonic pulsed waterjet peened Al-alloy/AlN composite, *Surf. Coatings Technol.* 448 (2022), 128915, <https://doi.org/10.1016/j.surfcoat.2022.128915>.
- [32] M.Y. Amegadzie, E.D. Moreau, B. Christensen, I.W. Donaldson, A. Tieu, M.M. Vijay, K.P. Plucknett, Ultrasonic pulsed waterjet surface peening of an industrial aluminum-based metal matrix composite, *Surf. Coatings Technol.* 426 (2021), 127795, <https://doi.org/10.1016/j.surfcoat.2021.127795>.
- [33] Y. Ma, Y. Zhang, J. Liu, L. Liu, J. Gong, Hard milling of carburized and waterjet peened 18CrNiMo7-6 steel, *Mach. Sci. Technol.* 25 (2020) 288–306, <https://doi.org/10.1080/10910344.2020.1815041>.
- [34] J.K. Cha, K. Paeng, U.W. Jung, S.H. Choi, M. Sanz, I. Sanz-Martín, The effect of five mechanical instrumentation protocols on implant surface topography and roughness: a scanning electron microscope and confocal laser scanning microscope analysis, *Clin. Oral Implants Res.* 30 (2019) 578–587, <https://doi.org/10.1111/clr.13446>.
- [35] H. Deppe, C. Wolff, F. Bauer, R. Ruthenberg, A. Sculean, T. Mücke, Dental implant surfaces after insertion in bone: an in vitro study in four commercial implant systems, *Clin. Oral Investig.* 22 (2018) 1593–1600, <https://doi.org/10.1007/s00784-017-2262-4>.
- [36] P. Gehrke, E. Spanos, C. Fischer, H. Storck, F. Tebbel, D. Duddeck, Influence of scaling procedures on the integrity of titanium nitride coated CAD/CAM abutments, *J. Adv. Prosthodont.* 10 (2018) 197–204, <https://doi.org/10.4047/jap.2018.10.3.197>.
- [37] M. Kunrath, R. dos Santos, S. de Oliveira, R. Hubler, P. Sesterheim, E. Teixeira, Osteoblastic cell behavior and early bacterial adhesion on macro-, micro-, and nanostructured titanium surfaces for biomedical implant applications, *Int. J. Oral Maxillofac. Implants* 35 (2020) 773–781, <https://doi.org/10.11607/jomi.8069>.
- [38] R. Melentiev, C. Kang, G. Shen, F. Fang, Study on surface roughness generated by micro-blasting on Co-Cr-Mo bio-implant, *Wear* 428–429 (2019) 111–126, <https://doi.org/10.1016/j.wear.2019.03.005>.
- [39] M. Menini, F. Pera, F. Bagnasco, F. Delucchi, E. Morganti, L. Canullo, P. Pesce, Morphological and chemical characterization of titanium and zirconia dental implants with different macro- and micro-structure, *Appl. Sci.* 10 (2020) 7520, <https://doi.org/10.3390/app10217520>.
- [40] G.A.F. Silva, F. Faot, W.J. da Silva, A.A. Del Bel Cury, Does implant surface hydrophilicity influence the maintenance of surface integrity after insertion into low-density artificial bone? *Dent. Mater.* 37 (2021) e69–e84, <https://doi.org/10.1016/j.dental.2020.10.024>.
- [41] M. Nalbant, H. Gökkaya, G. Sur, Application of Taguchi method in the optimization of cutting parameters for surface roughness in turning, *Mater. Des.* 28 (2007) 1379–1385, <https://doi.org/10.1016/j.matdes.2006.01.008>.
- [42] S.H. Tang, Y.J. Tan, S.M. Sapuan, S. Sulaiman, N. Ismail, R. Samin, The use of Taguchi method in the design of plastic injection mould for reducing warpage, *J. Mater. Process. Technol.* 182 (2007) 418–426, <https://doi.org/10.1016/j.jmatprotec.2006.08.025>.
- [43] R. Pareek, J. Bhamniya, Optimization of Injection Moulding Process using Taguchi and ANOVA, *Int. J. Sci. Eng. Res.* 4 (2013) 1–6.
- [44] H.J. Rack, J.I. Qazi, Titanium alloys for biomedical applications, *Mater. Sci. Eng. C.* 26 (2006) 1269–1277, <https://doi.org/10.1016/j.msec.2005.08.032>.
- [45] X. Liu, P.K. Chu, C. Ding, Surface modification of titanium, titanium alloys, and related materials for biomedical applications, *Mater. Sci. Eng. R Reports.* 47 (2004) 49–121, <https://doi.org/10.1016/J.MSER.2004.11.001>.
- [46] D. Duraccio, F. Mussano, M.G. Faga, Biomaterials for dental implants: current and future trends, *J. Mater. Sci.* 50 (2015) 4779–4812, <https://doi.org/10.1007/s10853-015-9056-3>.
- [47] K. Božić, M.M. Pavlović, G.M. Šekularac, S.V. Panić, M.R. Pantović Pavlović, Application aspects of joint anaphoresis/substrate anodization in production of biocompatible ceramic coatings, *J. Serbian Chem. Soc.* 88 (2023) 685–704, <https://doi.org/10.2298/JSC230118034B>.
- [48] M.R. Pantović Pavlović, N.L. Ignjatović, V.V. Panić, I.I. Mirkov, J.B. Kulaš, A. L. Malešević, M.M. Pavlović, Immunomodulatory effects mediated by nano amorphous calcium phosphate/chitosan oligosaccharide lactate coatings decorated with selenium on titanium implants, *J. Funct. Biomater.* 14 (2023), <https://doi.org/10.3390/jfb14040227>.
- [49] M.R. Pantović Pavlović, M.M. Pavlović, S. Eraković, T. Barudžija, J.S. Stevanović, N. Ignjatović, V.V. Panić, Relationship between the properties of an interlayer formed by in situ Ti anodization and anaphoretically deposited hydroxyapatite, *J. Serbian Chem. Soc.* 84 (2019) 1305–1318, <https://doi.org/10.2298/JSC190730105P>.
- [50] M.R. Pantović Pavlović, B.P. Stanojević, M.M. Pavlović, M.D. Mihailović, J. S. Stevanović, V.V. Panić, N.L. Ignjatović, Anodizing/anaphoretic electrodeposition of nano-calcium phosphate/chitosan lactate multifunctional coatings on titanium with advanced corrosion resistance, bioactivity, and antibacterial properties, *ACS Biomater. Sci. Eng.* 7 (2021) 3088–3102, <https://doi.org/10.1021/acsbomaterials.1c00035>.
- [51] D.R. Barjaktarević, V.R. Djokić, J.B. Bajat, I.D. Dimić, I.L. Cvijović-Alagić, M. P. Rakin, The influence of the surface nanostructured modification on the corrosion resistance of the ultrafine-grained Ti–13Nb–13Zr alloy in artificial saliva, *Theor. Appl. Fract. Mech.* 103 (2019), 102307, <https://doi.org/10.1016/j.tafmec.2019.102307>.
- [52] L. Huang, J. Folkes, P. Kinnell, P.H. Shipway, Mechanisms of damage initiation in a titanium alloy subjected to water droplet impact during ultra-high pressure plain waterjet erosion, *J. Mater. Process. Technol.* 212 (2012) 1906–1915, <https://doi.org/10.1016/j.jmatprotec.2012.04.013>.
- [53] International Organization for Standardization, ISO 25178-2: geometrical product specifications (GPS) - Surface texture: areal Part 2: terms, definitions and surface texture parameters, 2007.
- [54] K. Klauer, M. Eifler, J. Seewig, B. Kirsch, J.C. Aurich, Application of function-oriented roughness parameters using confocal microscopy, *Eng. Sci. Technol. Int. J.* 21 (2018) 302–313, <https://doi.org/10.1016/j.jestech.2018.04.004>.
- [55] W. Zielecki, P. Pawlus, R. Perłowski, A. Dzierwa, Surface topography effect on strength of lap adhesive joints after mechanical pre-treatment, *Arch. Civ. Mech. Eng.* 13 (2013) 175–185, <https://doi.org/10.1016/j.acme.2013.02.005>.
- [56] G.R.M. Matos, Surface roughness of dental implant and osseointegration, *J. Maxillofac. Oral Surg.* 20 (2021) 1–4, <https://doi.org/10.1007/s12663-020-01437-5>.
- [57] M. Taro, T. Chaise, D. Nélias, A methodology to predict the roughness of shot peened surfaces, *J. Mater. Process. Technol.* 217 (2015) 65–76, <https://doi.org/10.1016/j.jmatprotec.2014.10.016>.
- [58] N. Huber, J. Heerens, On the effect of a general residual stress state on indentation and hardness testing, *Acta Mater.* 56 (2008) 6205–6213, <https://doi.org/10.1016/j.actamat.2008.08.029>.
- [59] T.Y. Tsui, W.C. Oliver, G.M. Pharr, Influences of stress on the measurement of mechanical properties using nanoindentation: part I. Experimental studies in an aluminum alloy, *J. Mater. Res.* 11 (1996) 752–759, <https://doi.org/10.1557/JMR.1996.0091>.
- [60] K.L. Johnson, *Contact Mechanics*, Cambridge University Press, Cambridge, 1989, <https://doi.org/10.1201/b17588-12>.
- [61] W. Guo, H. Wang, P. Peng, B. Song, H. Zhang, T. Shao, H. Huan, H. Qiao, G. Qu, D. Zhu, J. Yan, Effect of laser shock processing on oxidation resistance of laser additive manufactured Ti6Al4V titanium alloy, *Corros. Sci.* 170 (2020), 108655, <https://doi.org/10.1016/j.corsci.2020.108655>.
- [62] Y. Zou, Y. Xu, J. Li, S. Liu, D. Wang, Y. Li, Evaluation of surface integrity in 18CrNiMo7-6 steel after multiple abrasive waterjet peening process, *Metals (Basel)* 10 (2020) 1–12, <https://doi.org/10.3390/met10060844>.
- [63] J. Shinjo, A. Umemura, Surface instability and primary atomization characteristics of straight liquid jet sprays, *Int. J. Multiph. Flow.* 37 (2011) 1294–1304, <https://doi.org/10.1016/j.ijmultiphaseflow.2011.08.002>.